Journal of
Materials Chemistry A

ROYAL SOCIETY
OF CHEMISTRY

PAPER

View Article Online
View Journal | View Issue

Cite this: *J. Mater. Chem. A*, 2025, **13**, 12566

Can dopants defend? Unraveling RuO_2 corrosion and reinforcement strategies for enhanced stability†

Badr Elkamash and Franziska Hess*

Received 9th January 2025
Accepted 25th March 2025

DOI: 10.1039/d5ta00218d

rsc.li/materials-a

To advance sustainable green hydrogen production through water electrolysis, where ruthenium dioxide (RuO_2) is a promising catalyst for the oxygen evolution reaction (OER), we investigate the stability of RuO_2, focusing on corrosion resistance – a key challenge limiting its practical application. Using density functional theory (DFT), we analyze the thermodynamic stability and reaction pathways across various RuO_2 surface orientations, with a primary focus on the (110) surface. Specifically, we assess the impact of doping with Ta, W, Re, Ir, Ti, and Pt on the thermodynamic stability of the $RuO_2(110)$ surface against dissolution of Ru surface atoms in the form of RuO_4. Our findings reveal that dopants Ir, Ti, and Pt in low oxidation states significantly enhance the resistance of the $RuO_2(110)$ surface against corrosion, while Ta, W, and Re in high oxidation states destabilize the surface, promoting degradation. We also identify specific dopant sites, such as those next to or directly underneath the dissolving Ru atom, that contribute significantly to surface stability, providing a roadmap for optimizing RuO_2 catalysts. Additionally, we extend the investigation to reaction pathways towards the dissolution of the Ru atom by incorporating the effects of dopants, revealing that dopants not only alter the thermodynamic stability but also the reaction mechanism due to their different termination preferences. We establish a strong linear correlation between the Gibbs free energy of RuO_4 formation (ΔG_{tot}) and the free energy of the highest intermediate (ΔG_{max}), proposing ΔG_{tot} as a reliable descriptor for predicting the thermodynamic stability of doped RuO_2 surfaces against Ru dissolution. This allows for efficient computational screening of surface modifications, including dopant selection and surface orientation tuning, without requiring detailed knowledge of the entire stepwise mechanism toward the formation and removal of RuO_4. This insight enables efficient computational screening of dopants and surface modifications, providing a framework for optimizing RuO_2 catalysts to improve durability in electrochemical applications.

1 Introduction

The transition towards sustainable energy sources has prompted intensive research into technologies capable of efficiently converting renewable electricity into storable and transportable forms. Among these technologies, water electrolysis is a promising avenue for producing green hydrogen, a clean and versatile energy carrier capable of decarbonizing various sectors, including transportation, industrial processes, and energy storage.[1] Polymer electrolyte membrane (PEM) electrolyzers (see Fig. 1), in particular, have gained traction due to their ability to catalyze hydrogen production at the cathode with high efficiency.[2] However, the sluggish kinetics of the oxygen evolution reaction (OER) at the anode pose a significant barrier to achieving optimal performance in water electrolysis systems.[3]

Addressing the challenges associated with the OER is paramount for advancing the commercial viability and widespread adoption of water electrolysis technology. Ruthenium dioxide (RuO_2) has emerged as a promising catalyst for the OER, owing to its high activity and favorable electrochemical properties.[4]

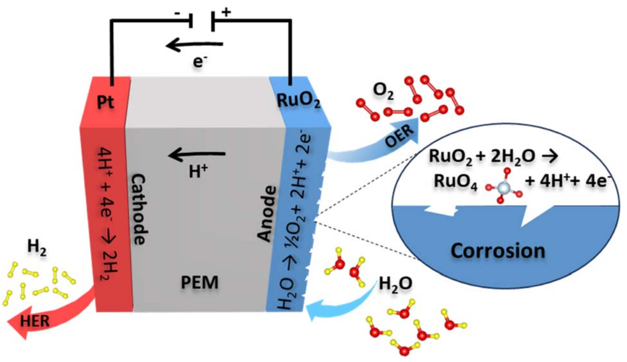

Fig. 1 A polymer electrolyte membrane (PEM) electrolyzer.

Institute for Chemistry, Technical University Berlin, D-10623 Berlin, Germany. E-mail: f.hess@tu-berlin.de

† Electronic supplementary information (ESI) available. See DOI: https://doi.org/10.1039/d5ta00218d

Despite its potential, the practical application of RuO_2 in water electrolysis is hindered by issues related to its stability under operating conditions.[5] The dissolution of Ru from the RuO_2 structure leads to the formation of soluble RuO_4 species, compromising the long-term stability and performance of RuO_2-based catalysts.[6–8] This instability is particularly pronounced at surface defect sites and undercoordinated Ru atoms, where dissolution is more likely to occur. Understanding the atomic-scale mechanisms of RuO_2 degradation is therefore essential for developing more stable catalyst formulations.

Enhancing the stability of RuO_2 requires a fundamental understanding of the mechanisms governing its degradation and the development of effective strategies to mitigate corrosion. One promising approach is heteroatom doping, where the incorporation of stable elements such as Ir, Ti, and Pt can modify the electronic structure of RuO_2, suppress Ru dissolution, and improve overall durability. For instance, a $Ru_{0.5}Ir_{0.5}$ alloy achieves four times higher stability compared to other Ru–Ir OER materials by adjusting surface composition through segregation.[9] In Ir–Ru mixed oxides, Ru dissolves more rapidly than Ir, leading to activity loss, while the corrosion resistance of Ir contributes to overall stability.[10] Titanium substitution in RuO_2 at low concentrations (12.5% and 20% Ti) enhances catalyst stability and reduces Ru dissolution.[11] $TiRuO_2$ solid solutions improve selectivity towards cathodic electrochemical reactions (CER), such as the hydrogen evolution reaction (HER), rather than enhance OER activity.

Another approach involves oxygen vacancy engineering, where dopants such as W and Er increase the formation energy of oxygen vacancies, effectively improving the structural integrity of RuO_2 and reducing dissolution in acidic PEM electrolyzers.[12] Furthermore, surface modifications, such as atomic layer deposition (ALD) of protective coatings and the formation of mixed-metal oxide layers, have been shown to enhance RuO_2 stability, with submonolayer IrO_x on RuO_2 significantly suppressing Ru dissolution and improving durability in PEM electrolyzers.[13] Meanwhile, Ru nanoparticles exhibit severe corrosion and instability during OER, whereas Ir nanoparticles show improved durability, indicating their potential as effective nanoscale OER catalysts.[14] Dispersing RuO_2 over defective TiO_2 enhances acidic OER performance by lowering the *OOH formation barrier and improving stability.[15]

In this study, leveraging Density Functional Theory (DFT) calculations in the computational hydrogen electrode model,[16,17] we investigate the thermodynamic stability and reaction pathways of RuO_2 catalysts in water electrolysis. We examine surface defects across various orientations, including (110), (100), $c(2 \times 2)$-reconstructed, and step edge configurations, to gain insights into the influence of surface morphology on RuO_2 stability against corrosion. Additionally, we explore the effects of support materials like M = (Ta, W, Re, Ir, Ti, and Pt), selected based on their stability in oxidative environments, electrochemical properties, and structural compatibility with RuO_2 due to their ability to form MO_2 rutile structures, thereby potentially forming stable solid solutions and interfaces with RuO_2. These elements are known to influence corrosion resistance, making them ideal candidates for this study. Their effects, either as a substrate or sublayer, on RuO_2 surface composition and stability are examined. Finally, we investigate how doping with a selection of these elements influences the thermodynamic stability of the $RuO_2(110)$ surface against corrosion.

In order to study the connection between thermodynamics and kinetics of corrosion, represented by the overall Gibbs free energy of RuO_4 formation (ΔG_{tot}) and the free energy of the highest intermediate (ΔG_{max}), we delve into the reaction pathways of RuO_4 formation at the bridge site of the (110) surface. Here, we focus on how different dopants alter the corrosion mechanisms and overall stability of RuO_2 surfaces. By detailing these reaction pathways, we aim to identify opportunities for optimizing RuO_2 catalysts to enhance their performance in water electrolysis. Finally, we demonstrate that ΔG_{max} is highly correlated with ΔG_{tot} for a large variety of modified surface structures, enabling the use of the Gibbs free energy of reaction as a descriptor in the optimization of the surface stability.

Ultimately, this study aims to advance sustainable energy technologies by developing robust and cost-effective catalysts for water electrolysis through knowledge-based proofing of the anode material against corrosion, facilitating the efficient use of renewable energy resources for green hydrogen production.

2 Computational details

Our investigation, grounded in DFT calculations, utilizes the Vienna *ab initio* simulation package (VASP)[18,19] employing the Perdew–Burke–Ernzerhof (PBE) functional.[20]

For surface computations, a $(4 \times 2 \times 1)$ k-point mesh is employed for (2×2) superstructures of the (110) surface, with a constant k-point density in reciprocal space for larger surface configurations. These asymmetric slabs comprise five RuO_2 trilayers, with two fixed and three fully relaxed trilayers. The relaxed bulk lattice parameters used in the calculations are optimized for RuO_2, IrO_2, and TiO_2. Specifically, the lattice constants for RuO_2 are $a = b = 4.497$ Å and $c = 3.105$ Å, for IrO_2 they are $a = b = 4.499$ Å and $c = 3.146$ Å, and for TiO_2 the parameters are $a = b = 4.589$ Å and $c = 2.958$ Å. A vacuum layer of 17.359 Å is employed. An energy cutoff of 450 eV and convergence criteria of 10^{-6} eV for energy during structural optimization is specified. Pseudopotentials are utilized for various elements including Ru, Ti, Ir, W, Re, Pt, Ta, O, and H[19,21] designated as Ru_sv, Ti, Ir, W, Re_pv, Pt_pv, Ta_pv, O, H.

For Ti, a Hubbard coefficient U_H of 8 eV is implemented in the Generalized Gradient Approximation (GGA) calculation to accurately describe the localized nature of Ti d-electrons in the semiconductor, thereby improving the characterization of its electronic structure.[22–24] Other elements in the system did not require a U_H correction, as their electron interactions were sufficiently well-described by conventional DFT.

The reactions investigated in this study include the oxygen evolution reaction at the anode, represented by the following reaction:

$$H_2O \rightarrow \frac{1}{2} O_2 + 2H^+ + 2e^-.$$

The corrosion reaction at the anode is:

$$RuO_2 + 2H_2O \rightarrow RuO_4 + 4H^+ + 4e^-.$$

At the cathode, the hydrogen evolution reaction is represented by:

$$4H^+ + 4e^- \rightarrow 2H_2.$$

Our computational approach is based on the total free energy equation, following methodologies detailed in previous studies.[16,17,25] The free energy change for a particular configuration i, denoted as $\Delta G_i(U_{\text{SHE}},_{\text{pH}})$, is calculated using the following expression:

$$\begin{aligned}\Delta G_i(U_{\text{SHE}}, \text{pH}) = {} & E_i^{\text{DFT}} - E_{\text{ref}}^{\text{DFT}} + n_{\text{RuO}_4} G_{\text{RuO}_4,\text{aq}} - n_{\text{e}^-,i} U_{\text{SHE}} \\ & -0.059\ \text{eV} \cdot n_{\text{e}^-,i} \cdot \text{pH} - n_{\text{H}_2\text{O},i} G_{\text{H}_2\text{O},l} \\ & + \frac{1}{2} n_{\text{H}_2,i} G_{\text{H}_2} + n_{\text{O}_2} G_{\text{O}_2} \end{aligned} \tag{1}$$

The reason RuO_4 was chosen in eqn (1) is that, at the potential corresponding to the dissolution threshold (around 1.21 V), RuO_4 is typically the dominant solvated species. At higher potentials, ruthenium tends to stabilize in its higher oxidation state, often as RuO_4. In this equation, $\Delta G_i(U_{\text{SHE}},_{\text{pH}})$ represents the free energy change for configuration i as a function of the applied potential relative to the standard hydrogen electrode (SHE), U_{SHE}, and the pH of the environment. The term E_i^{DFT} is the electronic energy of the system in configuration i, while $E_{\text{ref}}^{\text{DFT}}$ is reference energy, typically the energy of the initial state of the RuO_2 system, obtained from density functional theory (DFT) calculations. The numbers n_{RuO_4}, $n_{\text{e}^-,i}$, $n_{\text{H}_2\text{O},i}$, $n_{\text{H}_2,i}$, and n_{O_2} represent the number of RuO_4 units involved in the reaction or transformation for configuration i, the number of electrons transferred in the electrochemical process associated with configuration i, the number of adsorbed water molecules involved, the number of hydrogen molecules, and the number of oxygen molecules, respectively. The constant 0.059 eV represents a unit conversion factor at room temperature. U_{SHE} is the applied potential relative to the standard hydrogen electrode.

$G_{\text{RuO}_4,\text{aq}}$ is the free energy of RuO_4 in an aqueous solution, which can be determined using its entropy, $S_{\text{RuO}_4,\text{aq}} \approx 104.55$ J (K^{-1} mol^{-1}). G_{H_2} and G_{O_2} represent the free energies of hydrogen and oxygen molecules, respectively. The free energy of liquid water, $G_{\text{H}_2\text{O},l}$, is determined by the expression

$$G_{\text{H}_2\text{O},l} = E_{\text{H}_2\text{O},\text{g}}^{\text{DFT}} - T \cdot S_{\text{H}_2\text{O},\text{g}} + k_{\text{B}} T \ln(0.035) \tag{2}$$

where $S_{\text{H}_2\text{O},\text{g}} = 188.8$ J (K^{-1} mol^{-1}) is the entropy of gaseous water, calculated at room temperature $T = 298.15$ K, and 0.035 bar represents the vapor pressure of water.

At U_{corr}, which is the thermodynamic corrosion potential where the system is in dynamic equilibrium, and the net current of oxidation (corrosion) and reduction reactions on the surface is zero, indicating no net electron flow. When pH = 0, indicating an acidic environment, the total free energy at the corrosion potential is given by:

$$\begin{aligned}\Delta G_i(U_{\text{corr}}) = {} & E_i - E_{\text{ref}} + n_{\text{RuO}_4} G_{\text{RuO}_4,\text{aq}} - n_{\text{e}^-,i} U_{\text{corr}} \\ & - n_{\text{H}_4\text{O}} G_{\text{H}_2\text{O},l} + n_{\text{H}_2} G_{\text{H}_2} + n_{\text{O}_2} G_{\text{O}_2} = 0 \end{aligned} \tag{3}$$

This equation is essential for understanding the stability and reactivity of RuO_2 under different electrochemical conditions, providing insights into the factors influencing its performance as an oxygen evolution reaction (OER) catalyst.

3 Results

Our results are structured into two main parts: overall thermodynamic stability of Ru sites at the surface against RuO_4 formation and reaction pathways toward the dissolution of Ru in the form of RuO_4. This approach allows for a comprehensive analysis of RuO_2 surface corrosion, exploring both the inherent stability of various doped configurations and the specific mechanisms through which corrosion occurs. Finally, we examine the suitability of ΔG_{tot} as a descriptor for the stability of sites at the RuO_2(110) surface against corrosion by quantifying the correlation between ΔG_{tot}, representing the overall thermodynamic stability of a specific site, and ΔG_{max}, representing the least stable intermediate in the full corrosion mechanism.

3.1 Thermodynamic stability

In our investigation of the thermodynamic stability and corrosion susceptibility of various pure RuO_2 surfaces, we examined different orientations (110, 100, $c(2 \times 2)$-reconstructed (100), and RuO_2(110)/RuO_2(100) step edge) to discern their relative stability against corrosion. Subsequently, we examine the influence of dopants, as well as the direct and indirect effects of the catalyst support.

3.1.1 Different RuO_2 surface facets. The (110) surface of this material presents a nuanced picture with two distinct types of Ru atoms: coordinatively unsaturated sites (cus) and bridge sites (br). Fig. 2a and b show the free energy of corrosion as defined by eqn (3) as a function of the potential.

Positive free energies indicate that corrosion is not thermodynamically favored, implying that the surface is thermodynamically stable against corrosion. The potential at which the free energy turns negative will hereafter be referred to as the corrosion potential (U_{corr}), which indicates the lowest potential at which corrosion is thermodynamically preferred. Examining the corroded potential as a stability metric reveals variations in the stability of both atom types. The Ru_{br} site involves the removal of one Ru_{br} atom and one of its O_{br} atoms, while the other O_{br} atom relocates to the top of the nearest Ru_{br} atom, which then becomes $Ru_{5\text{f}}$. The corrosion potential of 1.277 V for the Ru_{br} site is higher than the bulk corrosion potential of 1.21 V (the bulk corrosion potential refers to the total conversion of bulk RuO_2 to RuO_4), indicating that the site remains stable, as corrosion is not thermodynamically favored at this higher potential.

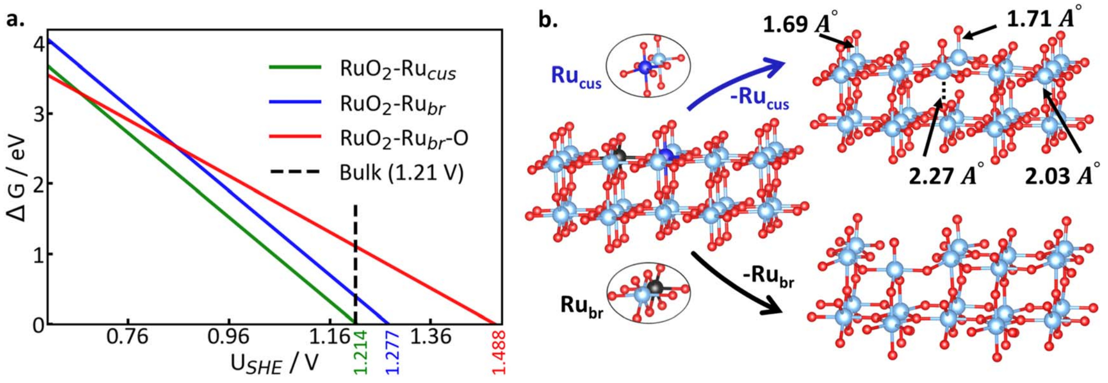

Fig. 2 Thermodynamic corrosion potentials and structures of (a and b) different Ru sites at the (110) surface. Corrosion potentials are 1.21 V, 1.277 V, and 1.488 V, calculated at pH = 0. Colors: sky blue: Ru_{bulk}, blue: Ru_{cus}, black: Ru_{br}, red: O.

The Ru_{br}–O site, formed by further removing the remaining O atom from the Ru_{br} site (which previously moved to the nearest Ru_{br} atom), transforms the nearest Ru_{br} atom into a Ru_{4f} atom without any termination on top. This site is identified as the most stable on the surface, with a corrosion potential of 1.488 V.

In contrast, the Ru_{cus} site is the least stable, indicating a higher susceptibility to corrosion. Its stability is comparable to that of bulk material, with a corrosion potential of 1.21 V. However, the instability of the Ru_{cus} site affects its neighboring Ru_{cus} atom, leading to the elongation of the underlying bond after metal dissolution, from 2.03 Å to 2.27 Å, as shown in Fig. 2b (top). In this specific case, our analysis reveals that the neighboring Ru_{cus} atom has a higher corrosion potential (1.291 V) compared to the initial Ru_{cus} site (1.214 V), making it less susceptible to dissolution.

We uncovered distinct dissolution behaviors and stabilities by extending our analyses to the (100) surface and step edge between the (100) and (110) facets. In each case, we examined the dissolution of different Ru sites with different oxygen terminations in the initial and final structures. Fig. 3 presents the summarized results, displaying the least stable site for each of the facets. Details for each of the facets can be found in Fig. S1–S3 in the ESI† for the (100), $c(2 \times 2)$-reconstructed (100) and (100)/(110) step edge, respectively. For instance, Fig. S1 in the ESI† illustrates the dissolution behavior of the (100) surface, revealing the formation of a tetrahedral Ru_{4f} structure post-dissolution and highlighting its comparatively lower stability: the least stable site on the (100) surface corrodes at a potential of 0.901 V, differing by 0.3 V compared to bulk RuO_2.

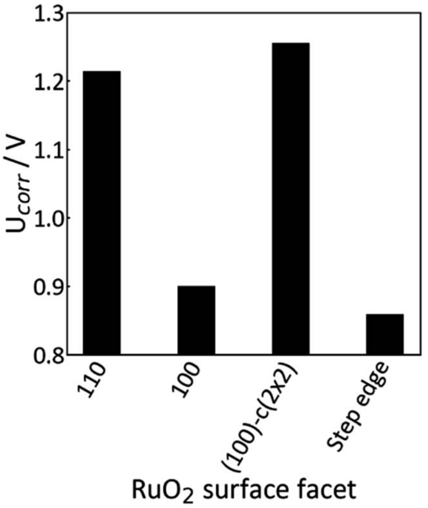

Fig. 3 Comparison of different RuO_2 surface facets based on potential calculations at pH = 0, identifying the least stable sites for each surface. The least stable sites are: 110: RuO_2-Ru_{cus}, 100: RuO_2-Ru_{surf}-2O, 100-$c(2 \times 2)$: RuO_2-Ru_{6f} + O_{ot}/Ru_{4f}, and step edge: RuO_2-Ru_{cus}-O.

Similarly, Fig. S2 in the ESI† elucidates the dissolution behavior of the (100)-$c(2 \times 2)$ surface, revealing corrosion potentials of 1.285 V for Ru_{4f} (reported by Hess and Over)[25] and 1.255 V for Ru_{6f} (according to our investigation). Ru_{4f}, Ru_{5f}, and Ru_{6f} denote distinct Ru crystallographic sites with fourfold, fivefold, and sixfold coordination, respectively, affecting the material's electronic structure and bonding.

Moving on to the dissolution behavior of step edge surfaces, Fig. S3 in the ESI† reveals corrosion potentials and stability characteristics. Notably, the step edge surface exhibits decreased stability compared to the bulk material, particularly evident in the least stable site (Ru_{cus}–O), with a corrosion potential of 0.858 V. The corrosion potentials for the least stable site on each facet are summarized in Fig. 3. This highlights the step edge as the least stable site among all examined, while the 110 surface emerges as one of the most stable surfaces. Consequently, we direct our further investigations towards the 110 surface.

3.1.2 RuO_2(110) surface with different dopants. To explore the potential improvement in stability against the RuO_2(110) surface corrosion, we investigated the impact of various dopants (Ta, W, Re, Ir, Pt, Ti) on its stability. The dopants were chosen based on their ability to form rutile-type structures, representing different groups of 3d and 5d transition metals. To isolate the effect of dopants from strain due to variation of the lattice parameter issues, we used the RuO_2 lattice parameter. Two models were constructed: (1) in the first model, a sublayer of dopants was placed in the middle of the RuO_2 layers, with the

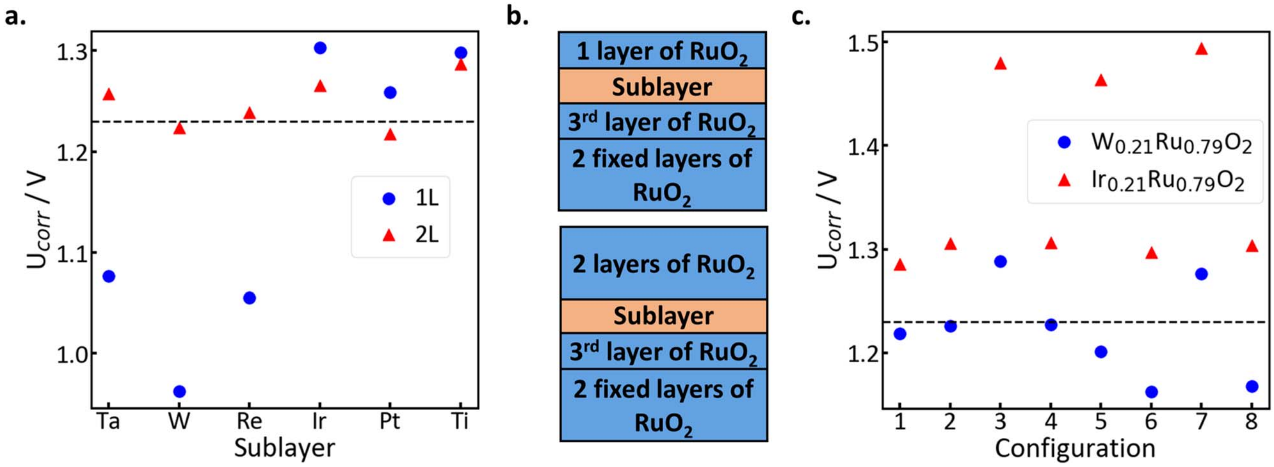

Fig. 4 (a and b) Influence of different dopant sublayers on RuO_2 corrosion with a varied thickness (1L or 2L) of RuO_2; (c) influence of different $M_{0.21}Ru_{0.79}O_2$ (M = Ir, W) configurations on RuO_2 corrosion (*cf.* Fig. S4†). Potentials were calculated at pH = 0.

two bottom layers fixed (atoms in the vertical direction were constrained), while the remaining layers were allowed to relax in all directions, (*cf.* Fig. 4b), and (2) random arrangement of dopants $M_{0.21}Ru_{0.79}O_2$ (M = Ir, W) on the metal sites. This approach allows us to solely observe the influence of dopants on the corrosion of the RuO_2 surface without introducing strain.

Furthermore, to distinguish the direct and indirect effect of the sublayer in RuO_2 corrosion, we deposited 1 or 2 layers of RuO_2 atop the dopant sublayer. In the case of 1 layer (1L), the corroded Ru atom is bonded to the sublayer *via* a single O_{3f} (direct effect), while with 2 layers (2L), only an indirect effect of the sublayer is probed, since surface Ru is not directly bonded to the sublayer. This approach enables us to investigate whether varying the thickness of the RuO_2 layer on the dopant sublayer affects the enhancement in stability against the $RuO_2(110)$ surface corrosion.

Fig. 4a and b illustrate the corrosion potential of the sublayer containing different dopants within the two models (1L, 2L). In the 1L model (direct effect), Ta, W, and Re destabilize the Ru top layer, whereas Ir, Pt, and Ti stabilize it against corrosion, as indicated by their decreased and increased corrosion potentials, respectively. The dopant is exposed after RuO_4 dissolution, resulting in different surface stabilities of the final surface: W strongly prefers a higher oxidation state, making it the least supportive dopant for RuO_2 surface stability against corrosion. Ta and Re prefer high oxidation states but not as strongly as W. In contrast, Ir, Pt, and Ti prefer lower oxidation states, with Ir and Ti being the most supportive dopants for RuO_2 surface stability against corrosion The trends within the two groups persist in the 2L model, but the corrosion potentials for each of the dopants now scatter closely around the value for pure RuO_2, with Ta, Ir, and Ti now causing a weak stabilization. For the others (W, Re, Pt), the effect on stability is negligible.

Continuing our investigation into the effect of doping on the stability of RuO_2 against corrosion, we selected W from the group (Ta, W, Re) and Ir from the group (Ir, Pt, Ti), mixing them randomly with RuO_2 to create eight configurations comprising a mixture of $M_{0.21}Ru_{0.79}O_2$ (M = Ir, W). To maintain consistency and avoid lattice parameter issues, we fixed two layers of pure RuO_2 at the bottom, while three layers of ($M_{0.21}Ru_{0.79}O_2$ (M = Ir, W)) were allowed to relax (the considered dopant configurations are shown in Fig. S4†). Fig. 4c displays the corrosion potential of these configurations. In all configurations, $Ir_{0.21}Ru_{0.79}O_2$ consistently demonstrates superior stability against corrosion compared to $W_{0.21}Ru_{0.79}O_2$. The observed variations in stability among configurations are fairly consistent between the two dopants, suggesting that the positions of dopant atoms influence the corrosion behavior of the Ru_{diss} atom, particularly its nearest neighbors. The distribution of dopant atoms in the bridge atom sites of the surface significantly influences stability, particularly the nearest bridge atom of Ru_{diss}, as observed in configurations (3, 5, 7), where the bridge site next to Ru_{diss} is occupied with a dopant atom. The metal atom directly underneath the Ru_{diss} plays a similarly strong role: configuration 7 in $Ir_{0.21}Ru_{0.79}O_2$, where Ir is the metal atom underlying Ru_{diss} atom, is identified as the most stable configuration. Conversely, configuration 3 in $W_{0.21}Ru_{0.79}O_2$, where Ru acts as the underlying Ru_{diss} atom, demonstrates the highest stability among $W_{0.21}Ru_{0.79}O_2$ configurations. This consistency aligns with sublayer results, where W and Ir in the sublayer destabilize and stabilize the surface Ru atom, respectively. This trend is equally observed in the random configurations. Conversely, configurations where the dopant is not located in the bridge position, such as configurations 6 and 8 in $W_{0.21}Ru_{0.79}O_2$, which lack W bridge atoms, are the least stable. This analysis provides valuable insights into predicting the stability of the surface based on specific dopant sites.

Interestingly, while in the case of Ir, all configurations demonstrate a stabilization, W can provide both a stabilizing effect, if it is located directly at the surface, and a destabilizing effect, if it is located in the sublayer. The strong role of the dopant distribution is further emphasized if we further consider different dopant contents, only favoring the most stabilizing patterns identified from the above analysis: in this approach, we can achieve a corrosion potential of 1.457 V for an Ir content as low as 8% in the slab, only placing one Ir atom in the bridge position next to, and another directly underneath (*cf.* Fig. S5†). This represents a significant enhancement compared to the bulk corrosion of 1.21 V. By adding more Ir dopants in favorable positions, the corrosion potential can be further raised to 1.492 V at 21% Ir in the slab. This result highlights that a significant degree of stabilization can theoretically be achieved by doping very little Ir in just the right positions; however, experimentally achieving such selective doping remains a significant challenge. This result is significant because the price of raw Ir metal has been over 10 times as high as that of Ru consistently over the past three years.[26] If Ir was used to stabilize RuO_2-based anodes for OER, its content should be as low as possible to reduce the cost of raw materials. Our results presented herein enable a knowledge-based approach to achieve these goals, which remains to be tested by experimental model studies.

3.1.3 Influence of strain and layer thickness in RuO_2@IrO_2(110) and RuO_2@TiO_2(110).

For further investigation, we selected Ir and Ti from the group (Ir, Pt, Ti) to create substrates of IrO_2 and TiO_2 (these being the most commonly used materials to modify RuO_2), aiming to explore additional parameters influencing the stability of the RuO_2(110) surface against corrosion. Here, we aim to elucidate the influence of a substrate on a pseudomorphically grown RuO_2 layer. In the substrate model, we focused on two aspects: first, the effect of RuO_2 thickness on its surface stability against corrosion of the RuO_2(110) surface, and second, the impact of strain due to the different lattice parameters on the stability against the RuO_2(110) surface corrosion. The lattice mismatch between RuO_2 and IrO_2 is approximately 0.839% along the [001] direction and −0.482% along the $[\bar{1}10]$ direction. Meanwhile, the mismatch between RuO_2 and TiO_2 is approximately −4.910% along the [001] direction and 2.496% along the $[\bar{1}10]$ direction, indicating that TiO_2 introduces a higher strain on RuO_2 compared to IrO_2.

Using the lattice parameter of IrO_2, Fig. 5a and b depict the corrosion potential of different thicknesses of RuO_2 on two IrO_2 substrate models consisting of either 3 or 4 layers (3L, 4L). We observe that there is a significant scatter in the U_{corr} for even and uneven numbers of RuO_2(110) layers. Similarly, we observe slightly different corrosion potentials for 3 and 4 layers of IrO_2 substrate. Both models consistently show that odd layers of RuO_2 stabilize the surface more strongly against even layers, and the corrosion potential converges around 6–7 layers to around 1.23 V for both models. According to these calculations, odd layers of RuO_2 grown on the IrO_2 clearly show a higher stabilization. Still, this behavior is likely significant only for very thin epitaxially grown layers not exceeding 4–5 layers. However, the lattice strain introduced due to IrO_2 as a substrate led to an overall stabilization of the RuO_2(110) surface by shifting the U_{corr} from 1.21 V (pure RuO_2(110)) to 1.23 V.

Such odd-even oscillations have been described previously for TiO_2(110),[27,28] and upon closer examination, we attribute it to the layer stacking in the (110) direction of the rutile lattice, which comprises two different types of atoms, Ru_{cus} and Ru_{br} stacked in an A–B–A–B sequence on the substrate. For odd and even layers, corrosion occurs in an A and B layer, respectively, which may explain the observed oscillation, although the exact reason for this behavior is still unknown. This observation prompted us to reinvestigate the (100) surface, composed solely of A layers, as depicted in Fig. S6.† In this model, the oscillation of the U_{corr} between odd and even layers is not observed. On a (100) surface, it is in steady observed that increasing thickness of strained RuO_2 on top of IrO_2, destabilizes the surface against corrosion, from 1.13 V (1L) to 0.84 V (7L). This indicates that strain can introduce a significant stabilizing effect in an otherwise inherently unstable facet like (100) and may be employed in addition to targeted doping to enhance the durability of RuO_2-based OER catalysts. On the other hand, in the more stable (110) facet, the effect of strain is negligible if IrO_2 is employed as a substrate.

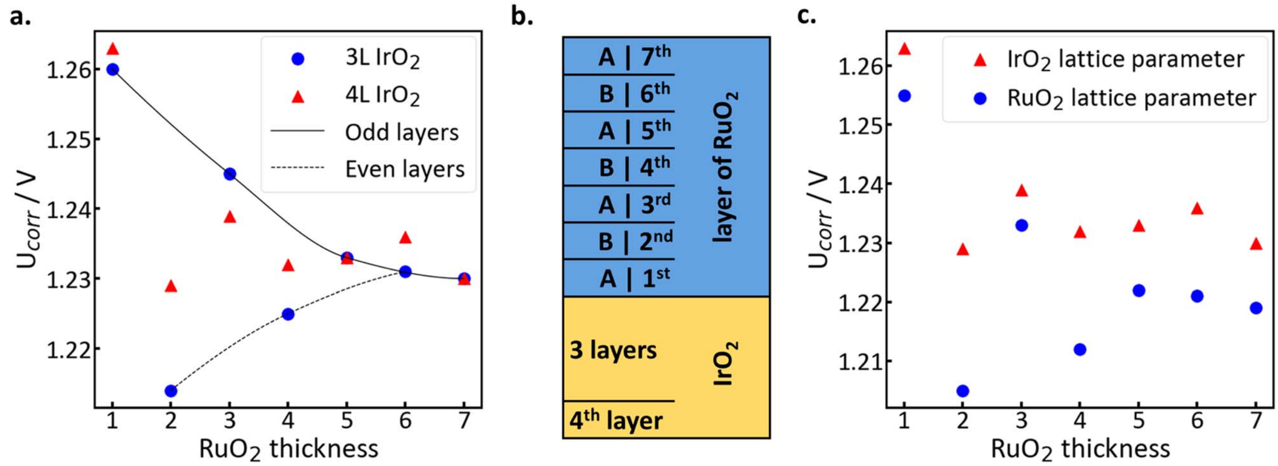

Fig. 5 (a and b) Influence of IrO_2(110) substrate with different thicknesses of RuO_2 on the stability of RuO_2 against corrosion (calculated with IrO_2 lattice parameter). Configurations include 3 or 4 layers of IrO_2 with 1–7 layers of RuO_2. (c) Influence of lattice parameters on the stability of RuO_2(110) against corrosion. Potentials were calculated at pH = 0.

To validate these conclusions, the corrosion potentials for RuO_2 layers grown on top of IrO_2 without strain (*i.e.*, employing the RuO_2 lattice parameter) are shown in Fig. 5c. Here, we observe the same odd-even oscillations; however, for thick RuO_2 layers, the corrosion potential converges to the value of pure $RuO_2(110)$, confirming that the stability of the RuO_2 surface is enhanced due to the strain introduced by the IrO_2 substrate. The oscillations, on the other hand, are not a result of strain, but occur in thin $RuO_2(110)$ layers regardless of strain. We emphasize that, despite these oscillations, the strain induced by the IrO_2 substrate enhances stability of $RuO_2(110)$, regardless of thickness.

For the TiO_2 substrate, we utilized the same model as for the 3L IrO_2 model. Fig. S7† depicts the corrosion potential of different thicknesses of RuO_2 on a 3L TiO_2 substrate with varying lattice parameters. The odd-even oscillation behavior occurs here as well, but with a lower intensity. Interestingly, when using the TiO_2 lattice parameter, the lattice strain leads to destabilization. Conversely, aligning with the RuO_2 lattice parameter results in slight stabilization, consistent with Section 3.1.2. The different stabilization behavior of IrO_2 and TiO_2 substrates is likely due to the different magnitude of lattice mismatch, but also due to the different orientations of strain and stress.

The investigation reveals that RuO_2 layers grown on IrO_2 substrates exhibit enhanced stabilization due to minimal lattice mismatch, while RuO_2 on TiO_2 substrates faces destabilization due to greater overall lattice mismatch, with odd-even oscillations in corrosion potential observed for both substrates in (110) direction. The (100) direction does not display such oscillations, but a significantly higher degree of stabilization due to the lattice mismatch.

3.2 Reaction pathways

In the second part of our investigation into the surface corrosion of the $RuO_2(110)$ surface, we examine the corrosion at the Ru_{br} site, which exhibits six-fold coordination at typical OER operating potentials. We follow the mechanism proposed by Liu *et al.*,[29] consisting of a stepwise addition of H_2O from the electrolyte, followed by the removal of proton/electron pairs, resulting in the transformation of octahedral RuO_6 into tetrahedral RuO_4, which subsequently detaches from the surface. Here, we investigate how a dopant sublayer, or quasi-random distribution of dopant atoms alter the energetics and reaction steps in the mechanism.

For the removal of Ru_{br}, we propose the following steps illustrated in Fig. 6, with the free energy profile depicted in Fig. 7:

Reconstruction step (a and b): this pivotal step initiates corrosion by lifting a Ru_{br} atom, forming two new Ru–O bonds with the neighboring O_{ot}. This Ru atom, now referred to as Ru_{diss}, requires +1.180 eV to accomplish this first, energetically uphill step.

First H_2O adsorption (c–g): in this step, an H_2O molecule is initially adsorbed on top of the new undercoordinated Ru site. This step is followed by the desorption of two-electron (e^-)–proton (H^+) pairs. The process begins with H_2O adsorption and progresses until only terminal oxygen remains. Consequently, the newly formed RuO_6 species undergoes a second reconstruction, transitioning into a tetrahedral RuO_4 species. During

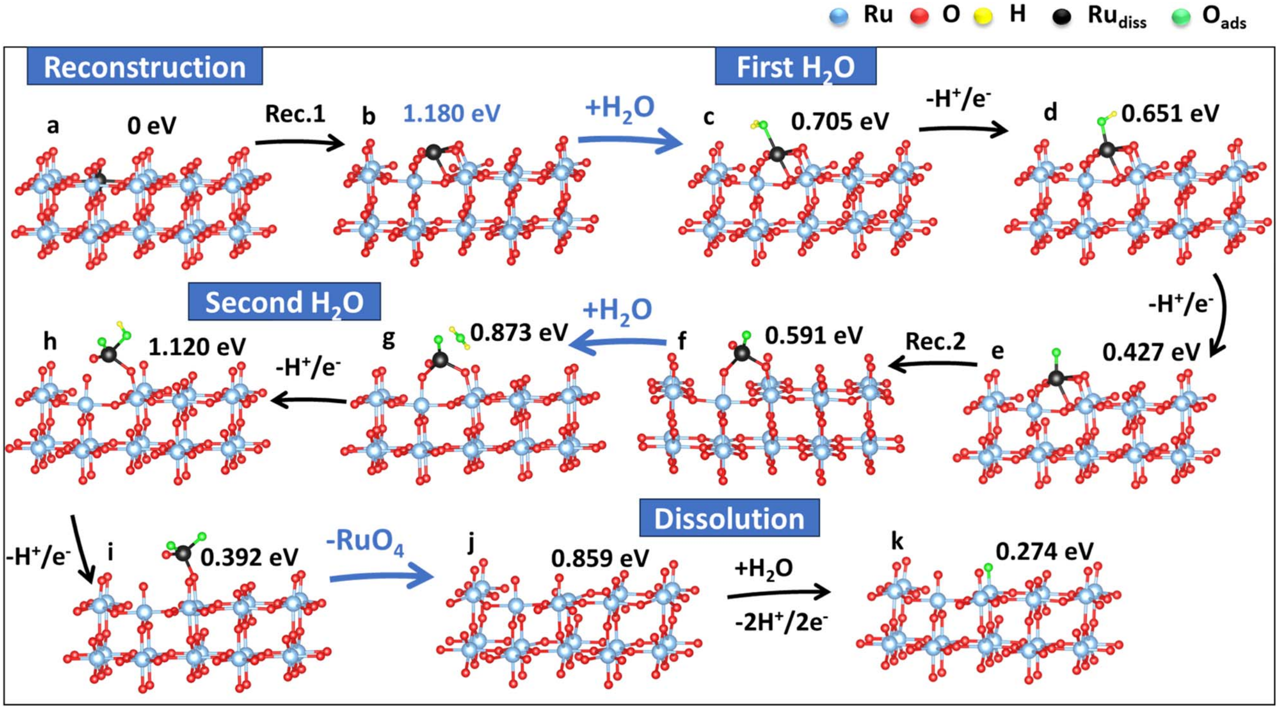

Fig. 6 The Ru_{br} corrosion mechanism on the $RuO_2(110)$. Colors: sky blue for Ru_{bulk}, red for O, yellow for H, black for Ru_{diss} (dissolution Ruthenium), and lime for O_{ads} (adsorbed oxygen).

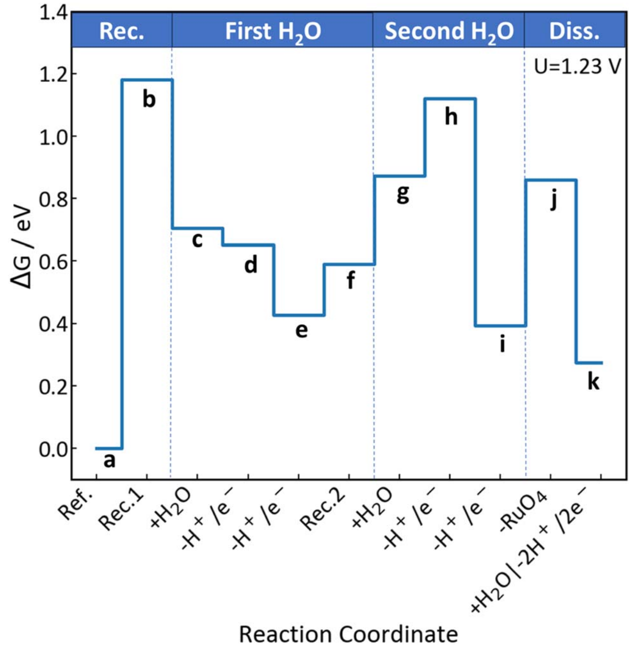

Fig. 7 The free energy profile of the Ru_{br} corrosion mechanism on the $RuO_2(110)$ surface at an electrode potential U_{SHE} = 1.23 V. Free energies were calculated at pH = 0.

this transformation, one of the O_{br} atoms detaches from the underlying Ru, becoming another terminal O. Simultaneously, the Ru_{diss} atom detaches from the underlying O_{3f} and one of the neighboring O_{ot} atoms. It is now connected to one O_{ot} and one O_{br}, establishing two terminal O atoms in a four-fold coordination (Ru_{4f}).

Second H_2O adsorption (h and i): mirroring the preceding step, a second H_2O molecule adsorbs. Upon the removal of the first H^+/e^- pair, the Ru_{diss} atom severs its bond to the neighboring O_{br}, forming a $RuO_3(OH)$ complex attached only to O_{ot}. The final removal of H^+/e^- is exergonic and leads to the formation of a RuO_4 species.

Dissolution step (j and k): in the final step, the RuO_4 detaches from the surface, leaving an empty Ru_{cus} site behind. Subsequently, this site is saturated by the adsorption of the final H_2O molecule and the detachment of two H^+/e^- pairs.

The free energy profile of the Ru_{br} corrosion mechanism on the $RuO_2(110)$ surface, as illustrated in Fig. 7, shows the free energy at each step. Notably, the initial reconstruction step (step b) presents the highest energetic threshold at 1.180 eV, indicating its unfavorable energetic characteristics. This chemical step is not influenced by the potential and likely represents the actual bottleneck under typical OER operating potentials.

Furthermore, removing the first H^+/e^- pair following the addition of the second H_2O (step h) is also quite high in free energy at 1.120 eV. This is the electrochemical step in nature, and its free energy can be lowered by increasing the applied potential. This indicates that the initially formed $RuO_3(OH)$/RuO_4 complexes may have a significant lifetime on the surface and may act as possible active sites in the OER, as proposed by Klyukin *et al.*[30]

We examined the influence of various dopants on the reaction pathway toward RuO_4 formation to gauge the potential enhancement in stability against $RuO_2(110)$ surface corrosion due to surface modification. Here, we distinguish between two possible modification strategies: (1) supporting RuO_2 on a substrate of a different oxide, for which we only consider Ir, as it has a similar lattice parameter to RuO_2, thereby avoiding strain effects, and (2) doping, *i.e.*, the quasi-random substitution of Ru ions by other ions, and the respective influence on the reaction steps of the corrosion mechanism. Here, we consider Ti, Ir, and W, as representatives of the three groups favoring different oxidation states as identified in Section 3.1.2.

3.2.1 Influence of substrate sublayer.

Initially, we scrutinized the mechanism of Ru_{br} removal over an $IrO_2(110)$ support substrate, utilizing three layers of IrO_2 with varying thicknesses of RuO_2. Based on our thermodynamic results (Fig. 5 and S7†), we selected a thickness of three layers to represent odd layers. Arguably, one layer shows a more pronounced change in stability due to the direct effect of the sublayer being exposed during the corrosion. This direct effect even changes the reaction mechanism in some cases, complicating the comparison. The direct effect of sublayer dopants will be considered separately in Section 3.2.2. Hence, we chose three layers to gauge the indirect effect of the support on the surface stability. Thermodynamically, we observed in Fig. 5 that odd and even layers lead to destabilization and stabilization compared to pure $RuO_2(110)$, respectively.

In Fig. 8, we illustrate the influence of the layer thickness on the free energy profile for the Ru_{br} corrosion mechanism on the $RuO_2@IrO_2(110)$ surface with two models (2L, 3L) of RuO_2. We observed a significant correlation between the thermodynamic free energy of corrosion (represented by the free energy difference between the final state k and initial state a in Fig. 8) and reaction mechanisms, represented by the free energy of the highest intermediate (ΔG_{max}). The reaction steps of corrosion on the supported $RuO_2(110)$ surfaces largely follow the same sequence as on pure $RuO_2(110)$, only the energies are shifted: The corrosion intermediates on odd layers exhibit higher free energies than their even-layer counterparts, indicating increased stability and reduced susceptibility to corrosion, both in terms of thermodynamics and in terms of thermodynamic barriers. However, the highest energetic threshold, *i.e.*, the reconstruction step (step b), remains unchanged for three layers of RuO_2 (green line), standing at 1.197 eV. For two layers of RuO_2 (orange line), the second H_2O adsorption, coupled with the removal of a proton/electron pair (step h) requires a free energy of 1.01 eV, which is not significantly different from the initial reconstruction step (step b), indicating a possible shift in the reaction pathway at this potential ($U_{SHE} = 1.23$ V). However, at a potential typically applied during OER ($U_{SHE} > 1.4$ V), the initial reconstruction step, being a purely chemical step, remains the highest energetic threshold.

3.2.2 Influence of randomly distributed dopants.

Continuing our investigation into the effects of dopants (Ti, Ir, W) on the reaction mechanisms, we arranged our investigation based on the surface termination preferences of cus sites at U_{SHE} = 1.23 V. Specifically, we examined the reactions

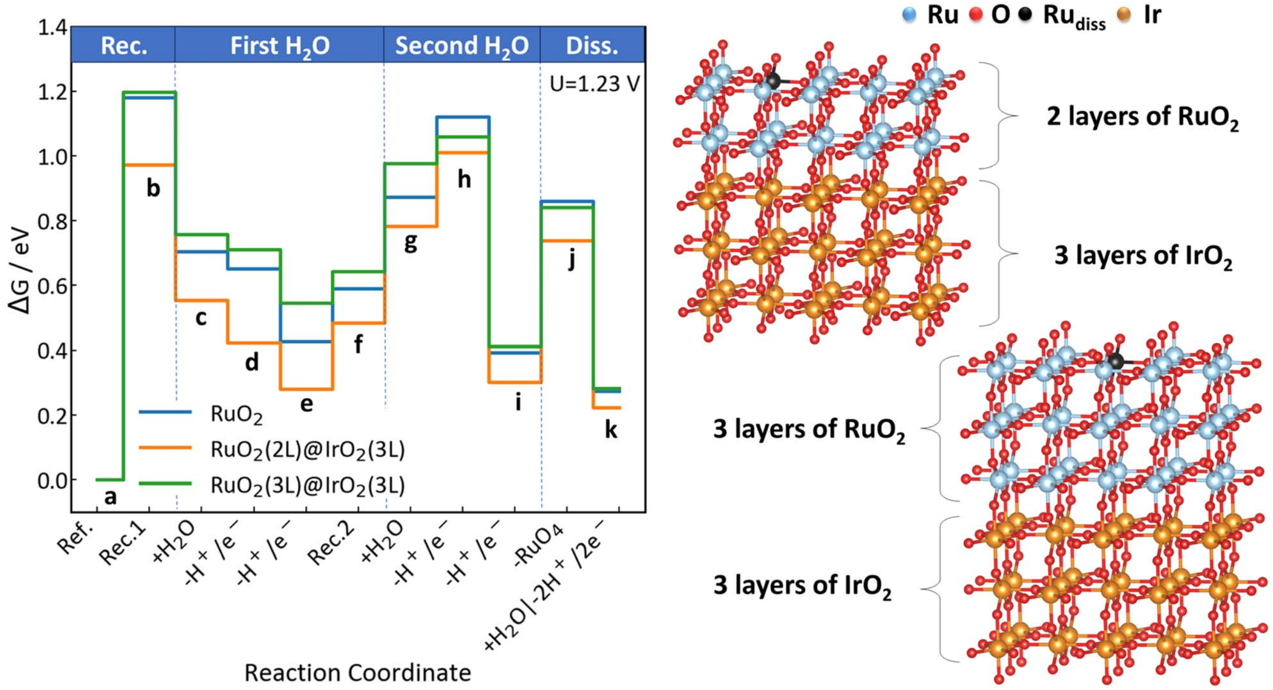

Fig. 8 Free energy profile at $U_{SHE} = 1.23$ V for Ru_{br} corrosion mechanism on RuO_2@IrO_2(110) surface, comparing 2L and 3L RuO_2 models. Free energies were calculated at pH = 0. Colors: sky blue for Ru_{bulk}, red for O, black for Ru_{diss}, and brown for Ir.

considering Ti, which favors termination without O; Ir, which favors termination with OH; and W, which favors O termination.

We initially focused on examining the $Ti_{0.67}Ru_{0.33}O_2$ mixture, maintaining two fixed layers of RuO_2 at the bottom while allowing three layers of $Ti_{0.67}Ru_{0.33}O_2$ to relax. Fig. 9 focuses on the impact of Ti atom distribution on the free energy profile of the Ru_{br} corrosion mechanism on the $Ti_{0.67}Ru_{0.33}O_2$(110) surface. We consider two different configurations, each defining a specific neighborhood around the dissolving Ru_{cus} atom, to elucidate the influence on individual reaction steps. In configuration 1, the bridge atom next to the

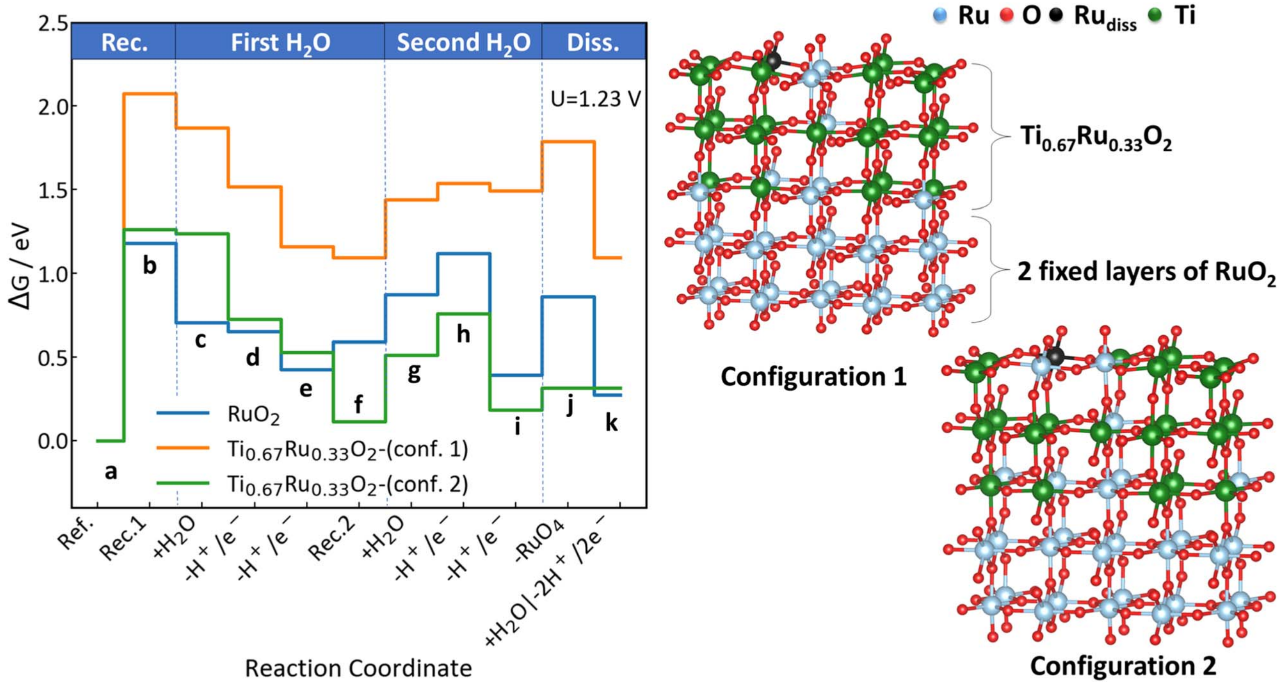

Fig. 9 The free energy profile at $U_{SHE} = 1.23$ V illustrates the Ru_{br} corrosion mechanism on the $Ti_{0.67}Ru_{0.33}O_2$(110) surface in two configurations. Free energies were calculated at pH = 0. Colors: sky blue for Ru_{bulk}, red for O, black for Ru_{diss}, and green for Ti.

dissolving atom is replaced by Ti, while the neighboring cus atom participating in the dissolution mechanism remain Ru. In configuration 2, the neighboring bridge atom remains Ru, while the neighboring cus atom is replaced by Ti. We note that, on these doped surfaces, there are many possible realizations of the corrosion mechanism, involving the bridge and cus sites, and in some cases, different cus sites. We tested multiple configurations and bond-breaking sequences to identify the pathways with the lowest free energy. This comparative analysis, illustrated in Fig. S9,† highlights key differences between chosen and non-chosen configurations, revealing how dopants can alter the reaction mechanism compared to pure $RuO_2(110)$. The results shown below reflect the most favorable pathways identified.

This specific modification of the environment alters the energetics of the reaction steps as follows: configuration 1 (orange line in Fig. 9) exhibits higher free energy and greater stability compared to pure RuO_2 (blue line) and configuration 2 (green line). The free energy reaches its maximum value of 2.075 eV in configuration 1 (orange line in Fig. 9) during the reconstruction step (step b), while configuration 2 reaches a maximum of 1.264 eV during the same step. Notably, in configuration 1, the nearest bridge neighbor to Ru_{diss} is Ti_{br}. During the reaction steps, especially in the second H_2O adsorption step (step h), no proton/electron pair is removed, and the H adsorbs onto O_{br} (which is on Ti_{br}). Then, in step j, the OH on Ti_{br} is removed.

In configuration 2, the nearest neighbor is another Ru_{br}. The transition from step a to step b, due to the unfavorable terminal O at Ti_{cus} in step a, involves three preparatory sub-steps (from b‴ to b' shown in detail in Fig. S8†). These sub-steps include the adsorption of H_2O on the Ti_{cus} atom. Upon the removal of the first H^+/e^- pair, the Ru_{diss} atom severs its bond to the neighboring OH of Ti_{cus}. The final removal of H^+/e^- is exergonic, resulting in the formation of the regular step b. Notably, we observed a significant drop in free energies, attributed to changes in the reaction mechanism compared to pure $RuO_2(110)$, starting from step f. Unlike pure RuO_2, where the tetrahedral RuO_4 species is connected to neighboring O_{br} and O_{ot}, in configuration 2, the RuO_4 species prefers being connected to two O_{ot}, resulting in an exergonic reaction step (e → f). This is mainly because it is highly unfavorable for Ti_{cus} to be capped by terminal oxygen; moving the RuO_4 species to the cus sites avoids this scenario. Similarly, upon the removal of the final H^+/e^- pair in the second H_2O adsorption step, the Ru_{diss} atom severs its bond with the neighboring O_{ot} of Ru_{cus} akin to the Walden inversion proposed by Hess *et al.*[25] This results in the formation of a RuO_4 species attached only to the O_{ot} of Ti_{cus}, thereby avoiding the unfavorable terminal O at Ti_{cus}. In the final step, RuO_4 detaches, leaving an empty Ti_{cus} site, as Ti_{cus} prefers termination without O.

Moving on to the $Ir_{0.67}Ru_{0.33}O_2$ mixture, we adopted a similar methodology by fixing two layers of RuO_2 at the substrate while allowing three layers of $Ir_{0.67}Ru_{0.33}O_2$ to relax. The distribution of Ir atoms in configurations 1 and 2 of $Ir_{0.67}Ru_{0.33}O_2$ mirrors that of Ti atoms in $Ti_{0.67}Ru_{0.33}O_2$.

Fig. 10 illustrates how the Ir distribution influences the free energy profile of the Ru_{br} corrosion mechanism on the $Ir_{0.67}Ru_{0.33}O_2(110)$ surface. Like in Fig. 9, we explore two configurations: configuration 1 (orange line) shows a ΔG_{max} of 2.248 eV during the dissolution step (step j), whereas configuration 2 (green line) peaks at 1.479 eV during the second H_2O

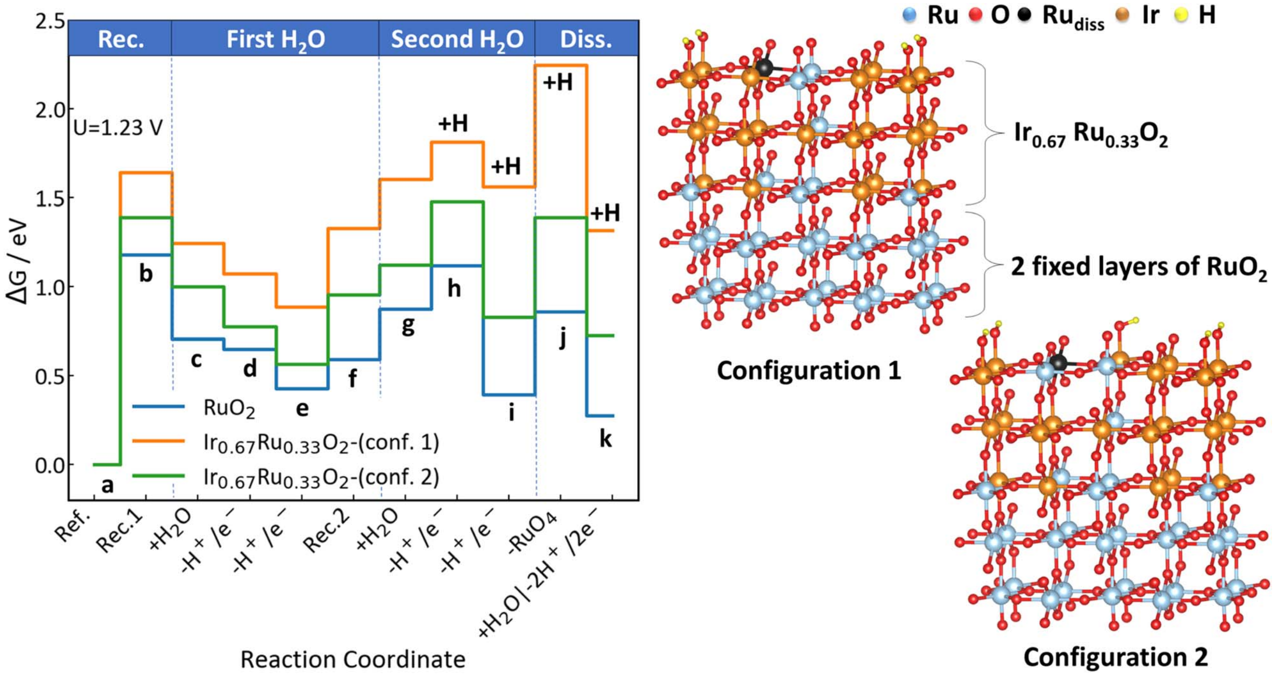

Fig. 10 The free energy profile at $U_{SHE} = 1.23$ V illustrates the Ru_{br} corrosion mechanism on the $Ir_{0.67}Ru_{0.33}O_2(110)$ surface for two configurations. Free energies were calculated at pH = 0. Colors: sky blue for Ru_{bulk}, red for O, yellow for H, black for Ru_{diss}, and brown for Ir.

adsorption step (step h). Configuration 1 exhibits higher free energy and greater stability compared to pure RuO_2 (blue line) and configuration 2. Notably, in configuration 1, the nearest neighbor to the Ru_{diss} is Ir_{br}. Starting from the second H_2O step (step h), upon the removal of the first H^+/e^- pair, the Ru_{diss} atom severs its bond with the neighboring O_{br}–Ir_{br}, resulting in the Ir_{br} being saturated by terminal OH. The subsequent steps take place exclusively on the cus sites. In configuration 2, the nearest neighbor is another Ru_{br}, and no changes in reaction mechanisms occur after step f, unlike configuration 2 of $Ti_{0.67}Ru_{0.33}O_2$.

Lastly, we investigated the $W_{0.21}Ru_{0.79}O_2$ mixture, employing the same layer arrangement as in the previous mixtures. Similar to the previous examinations, we chose two configurations: configuration 1, where the neighboring bridge and cus atoms are W and Ru, respectively, and *vice versa*, in configuration 2. We selected a lower doping content in this case because W is the least similar to Ru, and addition of too much dopant may alter the properties in unpredictable ways; nevertheless, significant effects are observed here, because the specific doped sites have a larger effect on the corrosion behavior than the overall doping content, as shown in Section 3.1.2.

Fig. 11 depicts how the W distribution influences the free energy profile of the Ru_{br} corrosion mechanism on the $W_{0.21}Ru_{0.79}O_2(110)$ surface. It explores two configurations relative to pure RuO_2. Notably, configuration 2 (green line) shows the highest free energy step at 1.144 eV during the final dissolution step (step j), while configuration 1 (orange line) peaks at 1.182 eV during the first reconstruction (step b).

The dramatic change in configuration 2 can be explained by the strong preference of W_{cus} to remain terminated by O at the given potential: upon the removal of the final H^+/e^- pair in the second H_2O step, the Ru_{diss} atom severs its bond with the neighboring O_{br} of Ru, forming a RuO_4 species attached only to the O_{ot} of W. While in the regular mechanism considered for all other cases, RuO_4 desorbs, along with the O_{ot}, W_{cus} requires to remain saturated. Therefore, before the dissolution step (step j), to lower this high free energy, a third H_2O molecule adsorbs, detaining two H^+/e^- pairs, as shown in Fig. S10.† This alteration in the mechanism akin to the Walden inversion proposed by Hess *et al.*[25] reduces the highest free energy step from 1.305 eV to 1.144 eV.

From the different behavior of the three dopants and their different termination preferences we learn that the choice of dopant can alter not only the free energies of the reaction steps, but also the nature of these steps. To avoid states that are too high in free energy due to unfavorable terminations of the metal sites next to Ru_{diss}, additional H_2O molecules may partake in the reaction toward RuO_4. On Ti-doped RuO_2, we observe that the initial reconstruction is complicated by the lack of terminal O at Ti_{cus}; however, the final states involving the removal of RuO_4 are simplified as they allow the Ti_{cus} to recover its vacant state. On the other hand, in W-doped RuO_2, W_{cus} has such a strong preference to be capped with O_{cus} that additional steps are required late in the mechanism to detach RuO_4 from the surface.

Close inspection of the data presented in Fig. 7–11 suggests that the thermodynamics of corrosion are highly correlated across a large variety of surface modifications. Based on all the data presented in this section, we quantitatively examined the correlation between the thermodynamic corrosion potential and the ΔG_{max} of the full reaction energy profiles to assess the

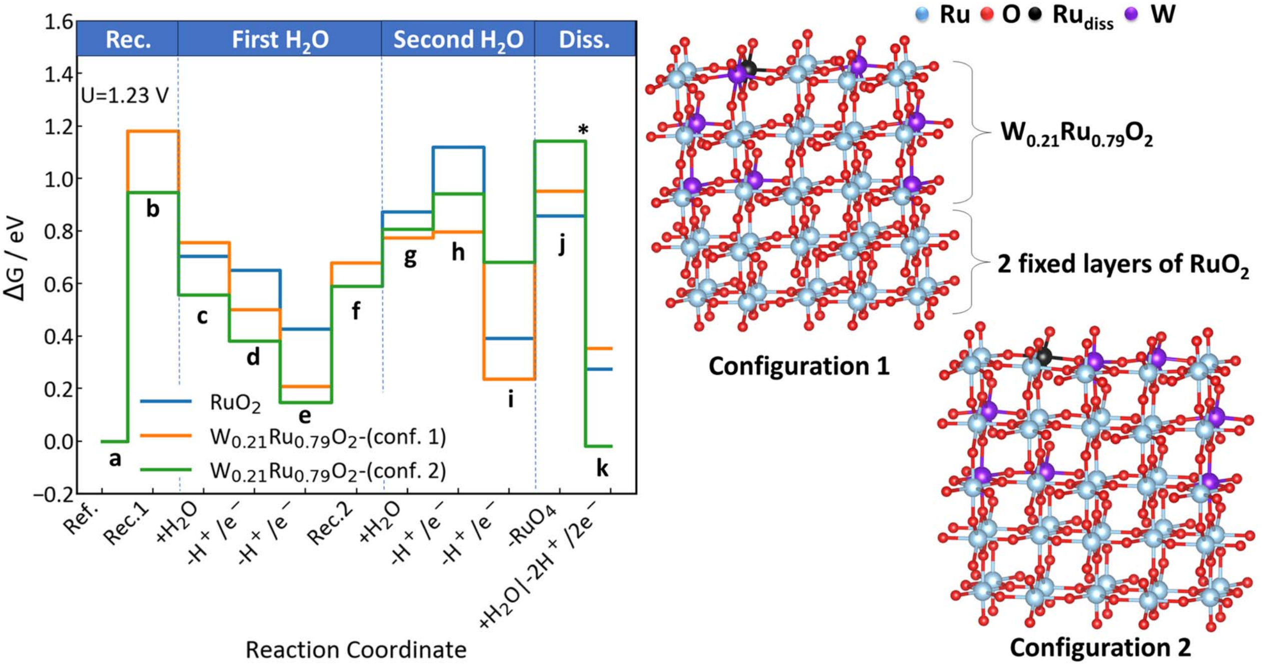

Fig. 11 The free energy profile at $U_{SHE} = 1.23$ V illustrates the Ru_{br} corrosion mechanism on the $W_{0.21}Ru_{0.79}O_2(110)$ surface for two configurations. Free energies were calculated at pH = 0. Colors: sky blue for Ru_{bulk}, red for O, black for Ru_{diss}, and violet for W. Note: step j consists of three steps represented by the highest free energy among them; please refer to Fig. S10† for details. *.

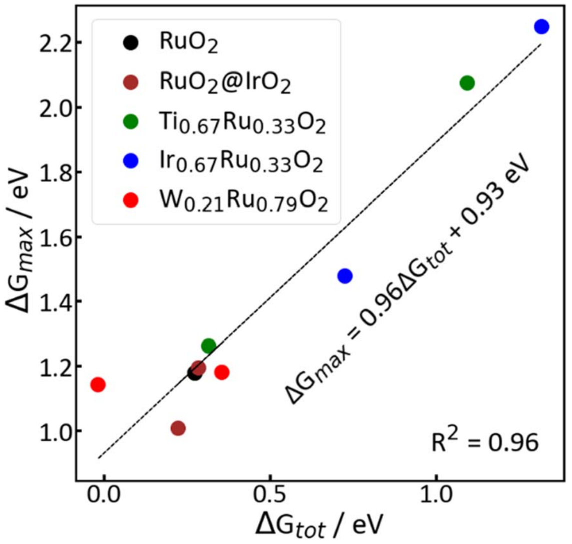

Fig. 12 Correlation between ΔG_{tot} and ΔG_{max} illustrates material stability interconnections across surfaces. Free energies were calculated at pH = 0 and $U_{\mathrm{SHE}} = 1.23$ V.

suitability of ΔG_{tot} as a descriptor for screening studies. As depicted in Fig. 12, our correlation analysis reveals a robust positive relationship ($R^2 = 0.96$) between the total free energy ($0 \leq \Delta G_{\mathrm{tot}} \leq 1.5$ eV) and the maximum free energy ($1.0\text{ eV} \leq \Delta G_{\mathrm{max}} \leq 2.2$ eV). This finding provides compelling evidence of the inherent connection between these parameters, highlighting a fundamental relationship governing material stability across diverse surface configurations across a large range of free energies. The maximum free energy (ΔG_{max}) is particularly significant for kinetic studies as it often represents the potential-determining step of a reaction, thus influencing the overall reaction rate and, in the case of corrosion, stability. Since ΔG_{tot} is a highly accessible quantity, requiring only the computation of initial and final state of the surface, we propose it as a descriptor suitable for screening the efficacy of different surface modifications *via* computation. Furthermore, this suggests that the stepwise corrosion mechanism does not need to be known in order to predict relative stabilities between similar surfaces.

Overall, our investigation into $Ti_{0.67}Ru_{0.33}O_2$, $Ir_{0.67}Ru_{0.33}O_2$, and $W_{0.21}Ru_{0.79}O_2$ mixtures unveils nuanced variations in reaction mechanisms and surface atom distributions. These findings underscore the critical role of dopant selection in optimizing RuO_2 surface stability against corrosion. By elucidating the intricate interplay between dopants, surface terminations, and reaction pathways, our study provides valuable insights for the design and engineering of advanced materials exhibiting long-term stability for applications ranging from catalysis to energy storage.

4 Discussion

To begin our discussion, we contextualize our investigation into the thermodynamic stability of the $RuO_2(110)$ surface within the broader scope of existing experimental and theoretical studies. Our investigation corroborates those of Over *et al.*,[31] who identified the $RuO_2(110)$ surface as the most stable among various facets. Additionally, our results are consistent with Hess *et al.*[25,32] on $RuO_2(100)$ and its $c(2 \times 2)$ reconstructed facets as detailed in Fig. 3. Stoerzinger *et al.*[33] also examined the oxygen evolution reaction (OER) activity across different facets (100), (110), (101), and (111), confirming that the (110) facet is the most stable, while the (100) facet is the most active. Our study specifically targets the stability of the $RuO_2(110)$ surface against corrosion and aims to enhance this stability.

Several studies have explored the incorporation of dopants into RuO_2 to improve stability. Kasian *et al.*[10] focused on the stabilization effect of Ir in RuO_2, demonstrating that incorporating 25% Ir significantly enhances stability. Similarly, Escalera-López *et al.*[34] investigated the electrochemical activity–stability relationship of Ir–Ru mixed oxides ($Ir_xRu_{1-x}O_2$), finding that 20% Ir improves stability while maintaining high activity. Both studies indicated a significant positive effect on surface stability with a slight decrease in activity, which informed our chosen Ir concentration in Fig. 4c. Our results are consistent with these findings, showing a significant improvement in the stability of the $RuO_2(110)$ surface. In studies exploring OER activity and electrocatalyst stability, $Ir_xRu_{1-x}O_y$ catalysts with Ir concentrations up to 70% were developed, achieving 3 A cm^{-2} at 1.8 V with strong stability in PEM electrolysis, though high turnover frequency altered Lewis acidity, impacting water oxidation.[35] Additionally, tuning the near-surface composition of Ru and Ir *via* surface segregation resulted in a $Ru_{0.5}Ir_{0.5}$ alloy exhibiting four times higher stability than the best Ru–Ir OER materials, without compromising catalytic activity.[9] This is consistent with our investigation of the $Ir_{0.67}Ru_{0.33}O_2$ mechanism, where the high Ir concentration contributes to one of the most stable surfaces, as shown in Fig. 10. We note that doping RuO_2 with Ir poses an economic challenge, as the high cost of Ir may limit practical application. Our findings indicate that substituting specific Ru sites by Ir may result in significant enhancement, an insight that could be exploited to reduce the Ir content of mixed $(Ru,Ir)O_2$ for OER applications.

Our study investigates the influence of lower cost doping elements, such as Ti and W, which have been proposed in the literature as potential dopants for RuO_2. Hao *et al.*[12] investigated the stability and activity of RuO_2 with W and Er ($W_{0.2}Er_{0.1}Ru_{0.7}O_{2-\delta}$). They found that adding W and Er significantly increases the catalyst's oxygen vacancy formation energy, improving durability and activity. This finding informed our chosen W concentration in Fig. 4c and 11 of the reaction mechanism investigation. Our predictions in Fig. 4c allow us to identify optimal dopant sites that enhance the durability and stability of the $M_{0.21}Ru_{0.79}O_2(110)$ surface.

For $Ti_xRu_{1-x}O_2$, Godínez-Salomón *et al.*[11] demonstrated that incorporating Ti (12.5–50%) enhances catalyst stability and reduces Ru dissolution, with low Ti concentrations (12.5–20 at%) significantly improving stability compared to pure RuO_2. Regarding IrO_2 substrates, most studies focus on RuO_2 substrates enhancing the surface activity of IrO_2. Our study uniquely examines the effect of RuO_2 thickness on an IrO_2

substrate, identifying the optimal thickness for maximal stability. Fig. 5 reveals a distinct odd-even layer behavior that suggests that uneven layers, such as 1 or 3, exhibit the highest stability.

Consistent with recent findings by Chaudhary *et al.*,[36] our study shows that tensile strain (as seen in RuO_2 on IrO_2) enhances corrosion resistance, while compressive strain (as observed in RuO_2 on TiO_2) leads to destabilization of the surface, highlighting the critical role of strain in influencing the corrosion behavior of RuO_2.

In terms of reaction mechanism, while many studies have concentrated on the oxygen evolution reaction (OER) mechanism at $RuO_2(110)$, fewer have delved into the specifics of RuO_2 corrosion mechanisms. Klyukin *et al.*[30] proposed a concept wherein a defect-free surface undergoes transitions leading to RuO_4 formation and subsequent corrosion. Similarly, Liu *et al.*[29] introduced four potential initial reconstruction steps (chemical steps), focusing on one to elucidate a mechanism that results in RuO_4 formation and surface corrosion. We adopted and expanded upon this mechanism in our investigation.

Our study extends beyond merely detailing the corrosion mechanisms of the RuO_2 surface to examine the impact of doping on these mechanisms, as shown in Fig. 8–11. Our findings highlight how the termination of the cus atoms in dopants affects the reaction mechanism and the associated free energies. In contrast to Gong *et al.*,[37] who use metal–oxygen bond strength from MD simulations to predict dissolution rates of complex glasses, our study focuses on thermodynamic descriptors, specifically $\Delta G_{\max}$ and ΔG_{tot}, to assess corrosion resistance in RuO_2. While Gong *et al.*[37] report R^2 values of 0.80–0.92 for bond strength and dissolution rates, our study finds a strong correlation ($R^2 = 0.96$) between $\Delta G_{\max}$ and ΔG_{tot}, demonstrating their effectiveness in predicting material stability. Similarly, Schwöebel *et al.*[38] use hydrogen bond acceptor strength as a descriptor for organic and inorganic compounds, demonstrating a high correlation ($R^2 = 0.97$) with experimental data, while our study employs thermodynamic parameters to predict corrosion stability, highlighting the broad applicability of descriptor-based methods across different material types. The concept of 'maximum free energy ($\Delta G_{\max}$)' as a descriptor for stability was first introduced by Exner and Over,[39] and our findings further support its utility in understanding reaction rates and mechanisms the trends of reaction rates and mechanisms upon altering the properties of the surface. Further work is required to understand the details of the kinetic processes governing the competition between the OER and the parasitic corrosion leading toward electrode dissolution. Kinetic studies are crucial for offering insights into activation energies, rate constants, and the effects of temperature and other reaction conditions.[40–51] Additionally, we plan to investigate the OER activity of various doped surfaces to compare their performance and stability relative to pure RuO_2.

5 Conclusion

Through comprehensive DFT analyses, we elucidate the stability and reaction mechanisms of RuO_2 catalysts in water electrolysis. Our investigation reveals the intricate interplay between surface orientations, dopants, and corrosion mechanisms, shedding light on key factors influencing RuO_2 stability against corrosion.

Our findings emphasize the critical role of understanding the intricate interplay between surface composition, dopants, and reaction mechanisms to optimize the stability of RuO_2 surfaces. Dopants such as Ir, Ti, and W exhibit diverse effects on stability, with Ir demonstrating superior stabilization compared to other elements. Specifically, Ti favors termination without O, Ir favors OH termination, and W favors O termination, each influencing distinct free energy profiles and reaction pathways, particularly evident in configuration 2 across all mixtures. Based on the correlation between the total change in Gibbs free energy (ΔG_{tot}) and the maximum Gibbs free energy ($\Delta G_{\max}$) we propose ΔG_{tot} as an accessible descriptor to predict the effect of different surface modifications on the stability of surface sites.

Overall, our study not only deepens our understanding of the complex behavior of RuO_2 surfaces but also offers valuable insights into designing tailored materials with enhanced stability for various applications, including catalysis and energy storage. These findings lay a solid foundation for future research aimed at optimizing the performance of RuO_2-based materials in real-world applications, thereby advancing the field of materials science and engineering.

Data availability

The Vienna *Ab initio* Simulation Package (VASP) code used in this study includes versions 5.4.4 and 6.4.2. Detailed information about VASP, including the latest updates and releases, can be found on the official VASP website: **https://www.vasp.at**.

Conflicts of interest

There are no conflicts to declare.

Acknowledgements

The authors thank the Deutsche Forschungsgemeinschaft and the DFG priority program SPP 2080 (DynaKat) for funding this project (Grant No. 493681475).

References

1 T. Audichon, T. W. Napporn, C. Canaff, C. Morais, C. Comminges and K. B. Kokoh, IrO_2 Coated on RuO_2 as Efficient and Stable Electroactive Nanocatalysts for Electrochemical Water Splitting, *J. Phys. Chem. C*, 2016, **120**, 2562–2573.

2 G. W. Crabtree, M. S. Dresselhaus and M. V. Buchanan, The Hydrogen Economy, *Phys. Today*, 2004, **57**, 39–44.

3 J. Masa, C. Andronescu and W. Schuhmann, Electrocatalysis as the Nexus for Sustainable Renewable Energy: The Gordian Knot of Activity, Stability, and Selectivity, *Angew. Chem., Int. Ed.*, 2020, **59**, 15298–15312.

4 J. Yu, Q. He, G. Yang, W. Zhou, Z. Shao and M. Ni, Recent Advances and Prospective in Ruthenium-Based Materials for Electrochemical Water Splitting, *ACS Catal.*, 2019, **9**, 9973–10011.

5 C. Spöri, J. T. H. Kwan, A. Bonakdarpour, D. P. Wilkinson and P. Strasser, The Stability Challenges of Oxygen Evolving Catalysts: Towards a Common Fundamental Understanding and Mitigation of Catalyst Degradation, *Angew. Chem., Int. Ed.*, 2017, **56**, 5994–6021.

6 S. Cherevko, S. Geiger, O. Kasian, N. Kulyk, J.-P. Grote, A. Savan, B. R. Shrestha, S. Merzlikin, B. Breitbach, A. Ludwig and K. J. Mayrhofer, Oxygen and hydrogen evolution reactions on Ru, RuO_2, Ir, and IrO_2 thin film electrodes in acidic and alkaline electrolytes: a comparative study on activity and stability, *Catal. Today*, 2016, **262**, 170–180.

7 R. Frydendal, E. A. Paoli, B. P. Knudsen, B. Wickman, P. Malacrida, I. E. L. Stephens and I. Chorkendorff, Benchmarking the Stability of Oxygen Evolution Reaction Catalysts: The Importance of Monitoring Mass Losses, *ChemElectroChem*, 2014, **1**, 2075–2081.

8 C. Roy, R. R. Rao, K. A. Stoerzinger, J. Hwang, J. Rossmeisl, I. Chorkendorff, Y. Shao-Horn and I. E. L. Stephens, Trends in Activity and Dissolution on RuO_2 under Oxygen Evolution Conditions: Particles *versus* Well-Defined Extended Surfaces, *ACS Energy Lett.*, 2018, **3**, 2045–2051.

9 N. Danilovic, R. Subbaraman, K. C. Chang, S. H. Chang, Y. Kang, J. Snyder, A. P. Paulikas, D. Strmcnik, Y. T. Kim, D. Myers, V. R. Stamenkovic and N. M. Markovic, Using Surface Segregation To Design Stable Ru-Ir Oxides for the Oxygen Evolution Reaction in Acidic Environments, *Angew. Chem., Int. Ed.*, 2014, **53**, 14016–14021.

10 O. Kasian, S. Geiger, P. Stock, G. Polymeros, B. Breitbach, A. Savan, A. Ludwig, S. Cherevko and K. J. J. Mayrhofer, On the Origin of the Improved Ruthenium Stability in RuO_2-IrO_2 Mixed Oxides, *J. Electrochem. Soc.*, 2016, **163**, F3099–F3104.

11 J. F. Godínez-Salomón, F. Ospina-Acevedo, L. A. Albiter, K. O. Bailey, Z. G. Naymik, R. Mendoza-Cruz, P. B. Balbuena and C. P. Rhodes, Titanium Substitution Effects on the Structure, Activity, and Stability of Nanoscale Ruthenium Oxide Oxygen Evolution Electrocatalysts: Experimental and Computational Study, *ACS Appl. Nano Mater.*, 2022, **5**, 11752–11775.

12 S. Hao, M. Liu, J. Pan, X. Liu, X. Tan, N. Xu, Y. He, L. Lei and X. Zhang, Dopants fixation of Ruthenium for boosting acidic oxygen evolution stability and activity, *Nat. Commun.*, 2020, **11**, 5368.

13 M. Escudero-Escribano, A. F. Pedersen, E. A. Paoli, R. Frydendal, D. Friebel, P. Malacrida, J. Rossmeisl, I. E. L. Stephens and I. Chorkendorff, Importance of Surface IrO_x in Stabilizing RuO_2 for Oxygen Evolution, *J. Phys. Chem. B*, 2017, **122**, 947–955.

14 T. Reier, M. Oezaslan and P. Strasser, Electrocatalytic Oxygen Evolution Reaction (OER) on Ru, Ir, and Pt Catalysts: A Comparative Study of Nanoparticles and Bulk Materials, *ACS Catal.*, 2012, **2**, 1765–1772.

15 X. Wang, X. Wan, X. Qin, C. Chen, X. Qian, Y. Guo, Q. Xu, W.-B. Cai, H. Yang and K. Jiang, Electronic Structure Modulation of RuO_2 by TiO_2 Enriched with Oxygen Vacancies to Boost Acidic O_2 Evolution, *ACS Catal.*, 2022, **12**, 9437–9445.

16 J. K. Nørskov, J. Rossmeisl, A. Logadottir, L. Lindqvist, J. R. Kitchin, T. Bligaard and H. Jónsson, Origin of the Overpotential for Oxygen Reduction at a Fuel-Cell Cathode, *J. Phys. Chem. B*, 2004, **108**, 17886–17892.

17 J. Rossmeisl, Z.-W. Qu, H. Zhu, G.-J. Kroes and J. Nørskov, Electrolysis of water on oxide surfaces, *J. Electroanal. Chem.*, 2007, **607**, 83–89.

18 G. Kresse and J. Furthmüller, Efficient iterative schemes for *ab initio* total-energy calculations using a plane-wave basis set, *Phys. Rev. B:Condens. Matter Mater. Phys.*, 1996, **54**, 11169–11186.

19 G. Kresse and D. Joubert, From ultrasoft pseudopotentials to the projector augmented-wave method, *Phys. Rev. B:Condens. Matter Mater. Phys.*, 1999, **59**, 1758–1775.

20 J. P. Perdew, J. A. Chevary, S. H. Vosko, K. A. Jackson, M. R. Pederson, D. J. Singh and C. Fiolhais, Atoms, molecules, solids, and surfaces: Applications of the generalized gradient approximation for exchange and correlation, *Phys. Rev. B:Condens. Matter Mater. Phys.*, 1992, **46**, 6671–6687.

21 P. E. Blöchl, Projector augmented-wave method, *Phys. Rev. B:Condens. Matter Mater. Phys.*, 1994, **50**, 17953–17979.

22 A. R. Fernández, A. Schvval, M. Jiménez, G. Cabeza and C. Morgade, Comparative study of the effect of the Hubbard coefficient U on the properties of TiO_2 and ZnO, *Mater. Today Commun.*, 2021, **27**, 102368.

23 E. German, R. Faccio and A. W. Mombrú, A DFT + U study on structural, electronic, vibrational and thermodynamic properties of TiO_2 polymorphs and hydrogen titanate: tuning the Hubbard 'U-term', *J. Phys. Commun.*, 2017, **1**, 055006.

24 V. I. Anisimov, J. Zaanen and O. K. Andersen, Band theory and Mott insulators: Hubbard U instead of Stoner I, *Phys. Rev. B:Condens. Matter Mater. Phys.*, 1991, **44**, 943–954.

25 F. Hess and H. Over, Coordination Inversion of the Tetrahedrally Coordinated Ru_{4f} Surface Complex on $RuO_2(100)$ and Its Decisive Role in the Anodic Corrosion Process, *ACS Catal.*, 2023, **13**, 3433–3443.

26 *Johnson Matthey*, https://matthey.com/products-and-markets/pgms-and-circularity/pgm-management, retrieved Aug. 9, 2024.

27 T. Bredow, L. Giordano, F. Cinquini and G. Pacchioni, Electronic properties of rutile TiO_2 ultrathin films: Odd-even oscillations with the number of layers, *Phys. Rev. B:Condens. Matter Mater. Phys.*, 2004, **70**, 035419.

28 Y.-B. Zhuang, R.-H. Bi and J. Cheng, Resolving the odd-even oscillation of water dissociation at rutile $TiO_2(110)$-water interface by machine learning accelerated molecular dynamics, *J. Chem. Phys.*, 2022, **157**, 164701.

29 W. Liu, Z. Duan and W. Wang, Water Oxidation-Induced Surface Reconstruction and Dissolution at the $RuO_2(110)$

Surface Revealed by First-Principles Simulation, *J. Phys. Chem. C*, 2023, **127**, 5334–5342.

30 K. Klyukin, A. Zagalskaya and V. Alexandrov, Role of Dissolution Intermediates in Promoting Oxygen Evolution Reaction at $RuO_2(110)$ Surface, *J. Phys. Chem. C*, 2019, **123**, 22151–22157.

31 H. Over, Surface Chemistry of Ruthenium Dioxide in Heterogeneous Catalysis and Electrocatalysis: From Fundamental to Applied Research, *Chem. Rev.*, 2012, **112**, 3356–3426.

32 F. Hess, S. Rohrlack, M. Knapp and H. Over, Evidence of a Tetrahedrally Coordinated RuO_4 Surface Complex on $RuO_2(100)$: Density Functional Theory and Beyond, *J. Phys. Chem. C*, 2022, **126**, 946–956.

33 K. A. Stoerzinger, O. Diaz-Morales, M. Kolb, R. R. Rao, R. Frydendal, L. Qiao, X. R. Wang, N. B. Halck, J. Rossmeisl, H. A. Hansen, T. Vegge, I. E. L. Stephens, M. T. M. Koper and Y. Shao-Horn, Orientation-Dependent Oxygen Evolution on RuO_2 without Lattice Exchange, *ACS Energy Lett.*, 2017, **2**, 876–881.

34 D. Escalera-López, S. Czioska, J. Geppert, A. Boubnov, P. Röse, E. Saraçi, U. Krewer, J.-D. Grunwaldt and S. Cherevko, Phase- and Surface Composition-Dependent Electrochemical Stability of Ir-Ru Nanoparticles during Oxygen Evolution Reaction, *ACS Catal.*, 2021, **11**, 9300–9316.

35 S. Siracusano, N. Hodnik, P. Jovanovic, F. Ruiz-Zepeda, M. Šala, V. Baglio and A. S. Aricò, New insights into the stability of a high performance nanostructured catalyst for sustainable water electrolysis, *Nano Energy*, 2017, **40**, 618–632.

36 P. Chaudhary, A. Zagalskaya, H. Over and V. Alexandrov, Strain-Dependent Activity-Stability Relations in RuO_2 and IrO_2 Oxygen Evolution Catalysts, *ChemElectroChem*, 2023, **11**, e202300659.

37 K. Gong and E. A. Olivetti, Development of structural descriptors to predict dissolution rate of volcanic glasses: Molecular dynamic simulations, *J. Am. Ceram. Soc.*, 2022, **105**, 2575–2594.

38 J. Schwöbel, R.-U. Ebert, R. Kühne and G. Schüürmann, Prediction of the Intrinsic Hydrogen Bond Acceptor Strength of Chemical Substances from Molecular Structure, *J. Phys. Chem. A*, 2009, **113**, 10104–10112.

39 K. S. Exner and H. Over, Kinetics of Electrocatalytic Reactions from First-Principles: A Critical Comparison with the *ab initio* Thermodynamics Approach, *Acc. Chem. Res.*, 2017, **50**, 1240–1247.

40 Y. Lee, C. Scheurer and K. Reuter, Epitaxial Core-Shell Oxide Nanoparticles: First-Principles Evidence for Increased Activity and Stability of Rutile Catalysts for Acidic Oxygen Evolution, *ChemSusChem*, 2022, **15**, e202300659.

41 Y. Lee, J. Timmermann, C. Panosetti, C. Scheurer and K. Reuter, Staged Training of Machine-Learning Potentials from Small to Large Surface Unit Cells: Efficient Global Structure Determination of the $RuO_2(100)$-$c(2 \times 2)$ Reconstruction and (410) Vicinal, *J. Phys. Chem. C*, 2023, **127**, 17599–17608.

42 F. Hess, Corrosion mechanism and stabilization strategies for RuO_2 and IrO_2 catalysts in the electrochemical oxygen evolution reaction, *Curr. Opin. Electrochem.*, 2023, **41**, 101349.

43 E. T. Bentria, P. M. Shenai, S. Sanvito, H. Park, L. K. Béland, N. Laycock and F. El Mellouhi, Computational demystification of iron carbonyls formation under syngas environment, *npj Mater. Degrad.*, 2024, **8**, 19.

44 A. S. Raman and A. Vojvodic, Providing Atomistic Insights into the Dissolution of Rutile Oxides in Electrocatalytic Water Splitting, *J. Phys. Chem. C*, 2022, **126**, 922–932.

45 C. F. Dickens and J. K. Nørskov, A Theoretical Investigation into the Role of Surface Defects for Oxygen Evolution on RuO_2, *J. Phys. Chem. C*, 2017, **121**, 18516–18524.

46 F. Hess, B. M. Smarsly and H. Over, Catalytic Stability Studies Employing Dedicated Model Catalysts, *Acc. Chem. Res.*, 2020, **53**, 380–389.

47 M. Carmo, D. L. Fritz, J. Mergel and D. Stolten, A comprehensive review on PEM water electrolysis, *Int. J. Hydrogen Energy*, 2013, **38**, 4901–4934.

48 R. Kötz, S. Stucki, D. Scherson and D. Kolb, *In situ* identification of RuO_4 as the corrosion product during oxygen evolution on ruthenium in acid media, *J. Electroanal. Chem. Interfacial Electrochem.*, 1984, **172**, 211–219.

49 K. Reuter and M. Scheffler, Composition, structure, and stability of $RuO_2(110)$ as a function of oxygen pressure, *Phys. Rev. B:Condens. Matter Mater. Phys.*, 2001, **65**, 035406.

50 A. Zagalskaya and V. Alexandrov, Role of Defects in the Interplay between Adsorbate Evolving and Lattice Oxygen Mechanisms of the Oxygen Evolution Reaction in RuO_2 and IrO_2, *ACS Catal.*, 2020, **10**, 3650–3657.

51 Y.-H. Fang and Z.-P. Liu, Mechanism and Tafel Lines of Electro-Oxidation of Water to Oxygen on $RuO_2(110)$, *J. Am. Chem. Soc.*, 2010, **132**, 18214–18222.